

Automated and objective removal of bifurcation aneurysms: incremental improvements, and validation against healthy controls

Original

Automated and objective removal of bifurcation aneurysms: incremental improvements, and validation against healthy controls / Bergersen, A.W., Chnafa, C., Gallo, D., Piccinelli, M., Steinman, D.A., Valen-Sendstad, K.. - In: JOURNAL OF BIOMECHANICS. - ISSN 0021-9290. - ELETTRONICO. - 96:(2019), p. 109342. [10.1016/j.jbiomech.2019.109342]

Availability:

This version is available at: 11583/2783974 since: 2020-01-22T10:34:05Z

Publisher:

Elsevier Ltd

Published

DOI:10.1016/j.jbiomech.2019.109342

Terms of use:

This article is made available under terms and conditions as specified in the corresponding bibliographic description in the repository

Publisher copyright

Elsevier postprint/Author's Accepted Manuscript

© 2019. This manuscript version is made available under the CC-BY-NC-ND 4.0 license
<http://creativecommons.org/licenses/by-nc-nd/4.0/>. The final authenticated version is available online at:
<http://dx.doi.org/10.1016/j.jbiomech.2019.109342>

(Article begins on next page)

Automated and Objective Removal of Bifurcation Aneurysms: Incremental Improvements, and Validation Against Healthy Controls

Aslak W. Bergersen^a, Christophe Chnafa^b, Diego Gallo^c, Marina Piccinelli^d, David A. Steinman^b, Kristian Valen-Sendstad^{a,*}

^aDepartment of Computational Physiology, Simula Research Laboratory, Lysaker, Norway

^bDepartment of Mechanical and Industrial Engineering, University of Toronto, Toronto, ON, Canada

^cDepartment of Mechanical and Aerospace Engineering, Politecnico di Torino, Torino, Italy

^dDepartment of Radiology and Imaging Sciences, Emory University, Georgia, USA

Abstract

Abnormal hemodynamic stresses are thought to correlate with aneurysm initiation, growth, and rupture. We have previously investigated the role of wall shear stress (WSS) and WSS gradients (WSSG) in search for a mechanistic link to formation of sidewall aneurysms using an automated and objective tool for aneurysm removal and arterial reconstruction in combination with computational fluid dynamics (CFD). However, we warned against the use of the tool for bifurcation type aneurysms because of a potential unrealistic reconstruction of the apex. We hypothesized that inclusion of additional morphological features from the surrounding vasculature could overcome these constraints. We extended the previously published method for removal and reconstruction of the bifurcation vasculature based on diverging and converging points of the parent and daughter artery centerlines, to also include two new centerlines between the daughter vessels, one of them passed through the bifurcation center. Validation was performed by comparing the efficacy of the two algorithms, using ten healthy models of the internal carotid artery terminus as ground truth. Qualitative results showed that the bifurcation apexes became smoother relative to the original algorithm; more consistent with the reference models. This was reflected quantitatively by a reduced maximum distance between the reference and reconstructed surfaces, although not statistically significant. Furthermore, the modified algorithm also quantitatively improved CFD derived WSS and WSSG, especially the latter. In conclusion, the modified algorithm does not perfectly reconstruct the bifurcation apex, but provides an incremental improvement, especially important for the derived hemodynamic metrics of interest in vascular pathobiology.

Keywords: Mechanobiology, Wall Shear Stress, Wall Shear Stress Gradients, Aneurysm Pathogenesis, Subarachnoid Hemorrhage

*For correspondence: Kristian Valen-Sendstad, Simula Research Laboratory, Lysaker, Norway. Email: kvs@simula.no

29 1. Introduction

30 Rupture of an intracranial aneurysm is the most common cause of subarachnoid hemorrhage (Wiebers et
31 al., 2003). The vast majority of aneurysms are asymptomatic and incidentally detected when patients undergo
32 neuroimaging for unrelated reasons. However, risk of clinical intervention can exceed the natural risk of rupture,
33 which is as low as 1% annually (Rinkel et al., 1998) making optimal patient-specific treatment decisions difficult.
34 Morphological indices have historically been used clinically for risk of rupture stratification (Raghavan et al.,
35 2005), but aneurysm morphology and size are ultimately surrogates for hemodynamically induced wall shear
36 stress (WSS) that contribute to vessel wall adaptation, remodeling, and vascular pathogenesis (Malek et al.,
37 1999; Morbiducci et al., 2016). Medical image-based computational fluid dynamics (CFD) (Taylor and
38 Steinman, 2010) has been extensively used in the investigation of vascular pathology, e.g., retrospectively
39 correlating flow phenotypes and stresses with aneurysm rupture status in search for prospective clinical
40 use (Xiang et al., 2011; Cebal et al., 2011).

41 However, 'predicting' aneurysm rupture status in large databases with a retrospectively known clinical
42 outcome can be problematic for a number of reasons. Aneurysm rupture is an event that may change
43 both morphology and size (Schneiders et al., 2014; Skodvin et al., 2017), only certain aneurysms have
44 endothelial cells (Frösen et al., 2004), and the aneurysm wall has a different structure compared to healthy
45 arteries (Canham et al., 1999). Additionally, there are uncertainties related to modeling of aneurysm flows,
46 like neck size overestimation with 3D rotational angiography (Schneiders et al., 2013), image segmentation,
47 which is both laborious and operator-dependent (Valen-Sendstad et al., 2018), and numerical solution
48 strategies (Valen-Sendstad and Steinman, 2014; Khan et al., 2015). Therefore, studying the fundamental role
49 of hemodynamics in aneurysms might be more intricate than originally anticipated. However, since the same
50 stimuli (WSS/WSSG) are believed to be involved in aneurysm initiation (Gao et al., 2008; Kulcsár et al.,
51 2011), growth (Sugiyama et al., 2012; Francis et al., 2013), and rupture (Cebal et al., 2005; Xiang et al.,
52 2011), one can investigate the hemodynamic stimulus and vascular response before aneurysms have formed,
53 without the aforementioned limitations. Hence, studying aneurysm initiation can provide mechanistic links
54 that are paramount for understanding fundamental vascular remodeling.

55 Ford et al. (Ford et al., 2009) developed a tool for objective aneurysm removal and arterial reconstruction
56 for investigating the plausible hemodynamic stimulus prior to sidewall aneurysm formation. They also warned
57 about the application to bifurcation aneurysms, and clearly stated that the tool 'remains to be verified'. The
58 latter is difficult because medical images of the pre-aneurysmal vasculature are rarely available. Secondly, the
59 high-resolution contrast-based computed tomography images needed to adequately reconstruct a bifurcation
60 apex, can naturally not be obtained from healthy individuals to limit potentially harmful radiation (Hendee
61 and O'Connor, 2012). From previous usage of the tool developed by Ford et al., for instance applied to
62 sidewall aneurysms Valen-Sendstad et al. (2014) we hypothesized that the bifurcation apex was occasionally
63 reconstructed with an artificial "notch" at the apex. We, therefore, proposed a technical improvement to the
64 original algorithm. We also acquired access to segmentation of intracranial blood vessels in ten patients that

65 underwent neurointensive care where no vascular abnormalities were found, which enabled validation. The
66 latter is indeed the only possible solution since the vasculature is unknown in the presence of an aneurysm,
67 which the algorithm actually is independent of. The aim of the study was to reconstruct an artificially
68 removed bifurcation, and compare the results of the two reconstruction algorithms to the reference and *a*
69 *priori* known bifurcation surface, especially focusing on relevant CFD derived stresses. In the following, we
70 will refer to the bifurcation surfaces as *reference*, *Ford*, and *modified* corresponding to the unmodified healthy
71 surface, the reconstructed surface from Ford et al., and our modified algorithm, respectively.

72 **2. Methods**

73 *2.1. Parent artery and bifurcation reconstruction*

74 We acquired access to 3D angiograms from ten patients that underwent neurointensive care where no
75 vascular abnormalities were found, originally collected for the open-source Aneurisk database, and subsequently
76 made publicly available (Aneurisk-Team, 2012). Figure 1 is adapted from Ford et al. and outlines the
77 algorithm for intracranial aneurysm removal and parent artery reconstruction. Note that we here illustrate
78 the algorithm using the same model as in Ford et al., but that we here apply the algorithm to models without
79 aneurysms only. Briefly, the algorithm is based on manipulating the Voronoi diagram, which is an alternative
80 representation of a surface (Piccinelli et al., 2009), and associated centerlines, to both remove and reconstruct
81 the bifurcation. Details are provided in the caption of Figure 1. The main difference between the original
82 and the modified algorithm is that the Voronoi diagram is interpolated onto two new centerlines between the
83 daughter vessels, these changes are colored purple in Figure 1.

84 *2.2. CFD, wall shear stress, and wall shear stress gradients*

85 CFD simulations were performed to investigate the effects of the reconstruction algorithms on hemodynamic
86 stresses. The Vascular Modelling ToolKit (Antiga et al., 2008) was used to extend the inlet and outlets five
87 times the local radius, and create meshes that on average consisted of three million tetrahedron cells with
88 four boundary layers, previously demonstrated to be sufficient to resolve WSS (Khan et al., 2015). Pulsatile
89 CFD simulations were performed assuming blood to behave as a Newtonian fluid (Khan et al., 2017) using
90 the *Oasis* solver (Mortensen and Valen-Sendstad, 2015), designed to obtain a solution that preserves kinetic
91 energy while minimizing numerical dispersion and diffusion errors, taking 10,000 time steps per cycle with a
92 period of 0.951s using an older adult waveform (Hoi et al., 2010). We specified a fully developed Womersley
93 velocity profile at the inlet and a time-averaged cross-sectional mean velocity of 0.27 *m/s* (Valen-Sendstad
94 et al., 2015) with a flow splitting approach for the outflow boundary as detailed in (Chnafa et al., 2018).

95 The efficacy of the reconstruction algorithms was quantified with respect to the mean and maximum
96 distance, curvature, WSS, and WSSG; measured relatively to the reference surface or associated CFD
97 simulations. All metrics were computed along the intersection between the objectively defined bifurcation
98 plane (Piccinelli et al., 2011) and surface, see white lines in Figure 3A, now referred to as *bifurcation lines*.

99 To quantitatively measure the differences, we sampled WSS and WSSG along the normalized bifurcation line,
100 and used a spline representation to compute the maximum curvature, a metric describing the bifurcation
101 apex "notch". A one-sided paired t-test was used to check if the modified method performed significantly
102 better, setting the level of significance to $p\text{-value} < 0.05$, not adjusting for multiple tests.

103 3. Results

104 3.1. Parent artery and bifurcation reconstruction

105 Figure 2 shows models 1-5 of the reference surface in white with the results of the original and modified
106 surface reconstruction algorithms colored in red in sub-plots A and B, respectively, all in opaque. We have
107 zoomed into model 1 to better highlight the differences. These qualitative results arguably show that the
108 modified algorithm produce reconstructed surfaces closer to the reference surface, most importantly at the
109 apex of the bifurcation. That is, the modified algorithm does not produce the same artificial "notch",
110 especially apparent in the models 1, 2, 4, and 5 shown in Figure 2A. The remaining five models are shown in
111 the Appendix with broadly consistent results.

112 3.2. Hemodynamic metrics: Wall shear stress and wall shear stress gradients

113 Focusing now on qualitative CFD derived results, Figure 3A shows bifurcation WSS maps obtained on
114 the modified, reference, and Ford surfaces, respectively. The WSS maps show largely similar global trends,
115 but with clearly visible differences at the bifurcation apex. This is further highlighted by the corresponding
116 WSS and WSSG values along the bifurcation lines shown in Figure 3B; especially WSSG is overestimated by
117 the original algorithm. The remaining five models are shown in the Appendix with broadly consistent results.

118 Table 1 shows quantitative results and demonstrates that both the curvature, WSS, and WSSG were
119 significantly closer to the reference values, with $p\text{-values} < 0.05$ marked in bold. The maximum distance
120 between the reference and reconstructed surfaces was also reduced with the modified algorithm, although not
121 statistically significant.

122 4. Discussion

123 We have shown that a minor modification of Ford et al.'s algorithm can reconstruct arterial bifurcations
124 that are more consistent with the reference bifurcation obtained from state-of-the-art medical images. As a
125 result, the computed WSS and WSSG from the reconstructed surfaces are statistically and phenotypically
126 improved compared to the original algorithm. Since the vast majority of aneurysms are located in bifurcations,
127 the modified algorithm could increase the number of subjects, increase the rigor of aneurysm initiation
128 research, and accelerate our understanding of fundamental vascular pathobiology. The latter can ultimately
129 contribute to further advances in research on aneurysm risk of rupture.

130 We have previously shown that there is relatively high intra- and interlaboratory uncertainty in segmenta-
131 tion of intracranial arteries (Valen-Sendstad et al., 2018). To reduce the uncertainty in the segmentation

132 we chose to focus on the ICA terminus since it is the largest intracranial artery, and is therefore the least
133 sensitive to segmentation errors because of the high voxel-to-vessel ratio. However, we have also compared
134 the geometrical metrics of middle- and anterior cerebral artery bifurcations and obtained equivalent results
135 for the maximum curvature (average absolute errors of 2.09 and 0.52 [$\frac{1}{mm}$] using the Ford and modified
136 algorithm, respectively, p-value < 0.001). These results, however, are associated with higher uncertainties
137 due to the smaller voxel-to-vessel ratio. Hence, a limitation is that validation has just been performed
138 on ten models. Another "feature" associated with the current methods is namely that neither algorithms
139 were designed or capable to reproduce a proximal stenosis, as observed in model 7, see Figure 5 of the
140 Appendix. Both algorithms produced a too wide arterial segment at the stenosis location, which resulted in a
141 lowered WSS/WSSG, relative to the reference model. The quantitative results are admittedly sensitive to the
142 bifurcation plane, as is obvious from Figures 3 and 5, however, they are objectively defined (Piccinelli et al.,
143 2011).

144 Relative to previous studies, our WSS/WSSG figures/lines appear to be noisier since we used human
145 "patient-specific" models instead of idealized (Kono et al., 2013; Lauric et al., 2018) or animal models (Meng
146 et al., 2010). We do not consider this a limitation, but rather a result of controlling numerical viscosity, and
147 the use of potentially "irregular" human models from the Aneurisk database. Smoothing the surfaces is
148 indeed possible, but we consider the current approach the most sensitive, and consequently the most rigorous
149 one.

150 Although we have shown that the modified algorithm better reconstructs the bifurcation, it still re-
151 mains to quote Ford et al., namely that users must still "exercise their judgment if a particular case
152 is a good candidate for similar studies". The code and associated tutorials are provided online, see
153 <https://github.com/KVSlab/morphMan>, which also includes other methods for objectively altering ad-
154 ditional morphological features of anatomically plausible vascular geometries.

155 5. Conclusion

156 We have shown that an incremental modification of Ford et al.'s aneurysm removal tools plausibly give
157 better agreement with the reference surface and the corresponding stresses on the arterial wall. The modified
158 algorithm can accelerate and broaden research on the hemodynamic stresses associated with aneurysm
159 initiation, with the ultimate extrapolation to rupture prediction.

160 6. Conflict of interest statement

161 The authors have no conflicts of interest to declare.

162 7. Acknowledgment

163 The study was supported by The Research Council of Norway through a Center of Excellence grant to the
164 Center for Biomedical Computing at Simula Research Laboratory, project number 179578. This work was

165 also carried out as a part of the Centre for Cardiological Innovation, and SIMMIS, project number 262827,
166 funded by the Research Council of Norway. Computations were performed on the GPC supercomputer at the
167 SciNet (Loken et al., 2010) HPC Consortium. SciNet is funded by: the Canada Foundation for Innovation
168 under the auspices of Compute Canada; the Government of Ontario; Ontario Research Fund - Research
169 Excellence; and the University of Toronto. Post processing was performed on the Abel Cluster, owned by the
170 University of Oslo and the Norwegian metacenter for High Performance Computing (NOTUR), and operated
171 by the Department for Research Computing at USIT, the University of Oslo IT-department, grant number
172 nn9316k.

173 8. References

- 174 Aneurisk-Team, 2012. AneuriskWeb project website, <http://ecm2.mathcs.emory.edu/aneuriskweb>. Web Site, accessed
175 01.08.2018.
- 176 Antiga, L., Piccinelli, M., Botti, L., Ene-Iordache, B., Remuzzi, A., Steinman, D. A., 2008. An image-based modeling
177 framework for patient-specific computational hemodynamics. *Medical & Biological Engineering & Computing*
178 46 (11), 1097–1112.
- 179 Canham, P. B., Finlay, H. M., Kiernan, J. A., Ferguson, G. G., 1999. Layered structure of saccular aneurysms assessed
180 by collagen birefringence. *Neurological Research* 21 (7), 618–626.
- 181 Cebal, J. R., Castro, M. A., Burgess, J. E., Pergolizzi, R. S., Sheridan, M. J., Putman, C. M., 2005. Characterization
182 of Cerebral Aneurysms for Assessing Risk of Rupture By Using Patient-Specific Computational Hemodynamics
183 Models. *American Journal of Neuroradiology* 26 (10), 2550–2559.
- 184 Cebal, J. R., Mut, F., Weir, J., Putman, C., 2011. Quantitative characterization of the hemodynamic environment in
185 ruptured and unruptured brain aneurysms. *American Journal of Neuroradiology* 32 (1), 145–151.
- 186 Chnafa, C., Brina, O., Pereira, V., Steinman, D., 2018. Better Than Nothing: A Rational Approach for Minimizing the
187 Impact of Outflow Strategy on Cerebrovascular Simulations. *American Journal of Neuroradiology* 39 (2), 337–343.
- 188 Ford, M. D., Hoi, Y., Piccinelli, M., Antiga, L., Steinman, D. A., 2009. An objective approach to digital removal of
189 saccular aneurysms: technique and applications. *The British Journal of Radiology* 82 (Special Issue 1), S55–S61.
- 190 Francis, S. E., Tu, J., Qian, Y., Avolio, A. P., 2013. A combination of genetic, molecular and haemodynamic risk
191 factors contributes to the formation, enlargement and rupture of brain aneurysms. *Journal of Clinical Neuroscience*
192 20 (7), 912–918.
- 193 Frösen, J., Piippo, A., Paetau, A., Kangasniemi, M., Niemelä, M., Hernesniemi, J., Jääskeläinen, J., 2004. Remodeling
194 of saccular cerebral artery aneurysm wall is associated with rupture: histological analysis of 24 unruptured and 42
195 ruptured cases. *Stroke* 35 (10), 2287–93.
- 196 Gao, L., Hoi, Y., Swartz, D. D., Kolega, J., Siddiqui, A., Meng, H., 2008. Nascent Aneurysm Formation at the Basilar
197 Terminus Induced by Hemodynamics. *Stroke* 39 (7), 2085–2090.
- 198 Hendee, W. R., O’Connor, M. K., 2012. Radiation risks of medical imaging: separating fact from fantasy. *Radiology*
199 264 (2), 312–321.
- 200 Hoi, Y., Wasserman, B. A., Xie, Y. J., Najjar, S. S., Ferruci, L., Lakatta, E. G., Gerstenblith, G., Steinman, D. A.,
201 2010. Characterization of volumetric flow rate waveforms at the carotid bifurcations of older adults. *Physiological*
202 *Measurement* 31 (3), 291.

- 203 Khan, M., Steinman, D. A., Valen-Sendstad, K., 2017. Non-Newtonian versus numerical rheology: Practical impact of
204 shear-thinning on the prediction of stable and unstable flows in intracranial aneurysms. *International journal for*
205 *numerical methods in biomedical engineering* 33 (7), e2836.
- 206 Khan, M., Valen-Sendstad, K., Steinman, D., 2015. Narrowing the expertise gap for predicting intracranial aneurysm
207 hemodynamics: impact of solver numerics versus mesh and time-step resolution. *American Journal of Neuroradiology*
208 36 (7), 1310–1316.
- 209 Kono, K., Masuo, O., Nakao, N., Meng, H., 2013. De novo cerebral aneurysm formation associated with proximal
210 stenosis. *Neurosurgery* 76 (6), E1080–E1090.
- 211 Kulcsár, Z., Ugron, A., Marosfői, M., Berentei, Z., Paál, G., Szikora, I., 2011. Hemodynamics of cerebral aneurysm
212 initiation: the role of wall shear stress and spatial wall shear stress gradient. *American Journal of Neuroradiology*
213 32 (3), 587–594.
- 214 Lauric, A., Greim-Kuczewski, K., Antonov, A., Dardik, G., Magida, J. K., Hippelheuser, J. E., Kono, K., Malek, A. M.,
215 2018. Proximal Parent Vessel Tapering is Associated With Aneurysm at the Middle Cerebral Artery Bifurcation.
216 *Neurosurgery*.
- 217 Loken, C., Gruner, D., Groer, L., Peltier, R., Bunn, N., Craig, M., Henriques, T., Dempsey, J., Yu, C.-H., Chen, J.,
218 et al., 2010. SciNet: lessons learned from building a power-efficient top-20 system and data centre. In: *Journal of*
219 *Physics: Conference Series*. Vol. 256(1). IOP Publishing, p. 012026.
- 220 Malek, A. M., Alper, S., Izumo, S., 1999. Hemodynamic Shear Stress and Its Role in Atherosclerosis. *JAMA* 282 (21),
221 2035–2042.
- 222 Meng, H., Natarajan, S., Gao, L., Ionita, C., Kolega, J., Siddiqui, A., Mocco, J., 2010. Aneurysmal changes at the
223 basilar terminus in the rabbit elastase aneurysm model. *American Journal of Neuroradiology* 31 (3), E35–E36.
- 224 Morbiducci, U., Kok, A. M., Kwak, B. R., Stone, P. H., Steinman, D. A., Wentzel, J. J., et al., 2016. Atherosclerosis
225 at arterial bifurcations: evidence for the role of haemodynamics and geometry. *Thrombosis and haemostasis* 115 (3),
226 484–492.
- 227 Mortensen, M., Valen-Sendstad, K., 2015. *Oasis*: A high-level/high-performance open source Navier–Stokes solver.
228 *Computer Physics Communications* 188, 177–188.
- 229 Piccinelli, M., Bacigaluppi, S., Boccardi, E., Ene-Iordache, B., Remuzzi, A., Veneziani, A., Antiga, L., 2011. Geometry
230 of the internal carotid artery and recurrent patterns in location, orientation, and rupture status of lateral aneurysms:
231 an image-based computational study. *Neurosurgery* 68 (5), 1270–85; discussion 1285.
- 232 Piccinelli, M., Veneziani, A., Steinman, D. A., Remuzzi, A., Antiga, L., 2009. A framework for geometric analysis of
233 vascular structures: application to cerebral aneurysms. *IEEE transactions on medical imaging* 28 (8), 1141–1155.
- 234 Raghavan, M. L., Ma, B., Harbaugh, R. E., 2005. Quantified aneurysm shape and rupture risk. *Journal of Neurosurgery*
235 102 (2), 355–62.
- 236 Rinkel, G. J. E., Djibuti, M., Algra, A., van Gijn, J., 1998. Prevalence and Risk of Rupture of Intracranial Aneurysms:
237 A Systematic Review. *Stroke* 29 (1), 251–256.
- 238 Schneiders, J., Marquering, H., Antiga, L., Van den Berg, R., VanBavel, E., Majoie, C., 2013. Intracranial aneurysm
239 neck size overestimation with 3D rotational angiography: the impact on intra-aneurysmal hemodynamics simulated
240 with computational fluid dynamics. *American Journal of Neuroradiology* 34 (1), 121–128.

- 241 Schneiders, J., Marquering, H., van den Berg, R., VanBavel, E., Velthuis, B., Rinkel, G., Majoie, C., 2014. Rupture-
242 Associated Changes of Cerebral Aneurysm Geometry: High-Resolution 3D Imaging before and after Rupture.
243 American Journal of Neuroradiology 35 (7), 1358–1362.
- 244 Skodvin, T. Ø., Johnsen, L.-H., Gjertsen, Ø., Isaksen, J. G., Sorteberg, A., 2017. Cerebral aneurysm morphology
245 before and after rupture: nationwide case series of 29 aneurysms. Stroke 48 (4), 880–886.
- 246 Sugiyama, S.-I., Meng, H., Funamoto, K., Inoue, T., Fujimura, M., Nakayama, T., Omodaka, S., Shimizu, H.,
247 Takahashi, A., Tominaga, T., 2012. Hemodynamic analysis of growing intracranial aneurysms arising from a
248 posterior inferior cerebellar artery. World Neurosurgery 78 (5), 462–8.
- 249 Taylor, C. A., Steinman, D. A., 2010. Image-based modeling of blood flow and vessel wall dynamics: applications,
250 methods and future directions. Annals of Biomedical Engineering 38 (3), 1188–1203.
- 251 Valen-Sendstad, K., Bergersen, A. W., Shimogonya, Y., Goubergrits, L., Bruening, J., Pallares, J., Cito, S., Piskin, S.,
252 Pekkan, K., Geers, A. J., et al., 2018. Real-world variability in the prediction of intracranial aneurysm wall shear
253 stress: the 2015 International Aneurysm CFD Challenge. Cardiovascular Engineering and Technology, 1–21.
- 254 Valen-Sendstad, K., Piccinelli, M., KrishnankuttyRema, R., Steinman, D. A., 2015. Estimation of Inlet Flow Rates
255 for Image-Based Aneurysm CFD Models: Where and How to Begin? Annals of Biomedical Engineering 43 (6),
256 1422–1431.
- 257 Valen-Sendstad, K., Piccinelli, M., Steinman, D. A., 2014. High-resolution computational fluid dynamics detects flow
258 instabilities in the carotid siphon: Implications for aneurysm initiation and rupture? Journal of Biomechanics
259 47 (12), 3210–3216.
- 260 Valen-Sendstad, K., Steinman, D. A., 2014. Mind the gap: impact of Computational Fluid Dynamics solution
261 strategy on prediction of intracranial aneurysm hemodynamics and rupture status indicators. American Journal of
262 Neuroradiology 35 (3), 536–543.
- 263 Wiebers et al., 2003. Unruptured intracranial aneurysms: natural history, clinical outcome, and risks of surgical and
264 endovascular treatment. The Lancet 362 (9378), 103–110.
- 265 Xiang, J., Natarajan, S. K., Tremmel, M., Ma, D., Mocco, J., Hopkins, L. N., Siddiqui, A. H., Levy, E. I., Meng, H.,
266 2011. Hemodynamic-Morphologic Discriminants for Intracranial Aneurysm Rupture. Stroke 42 (1), 144–152.

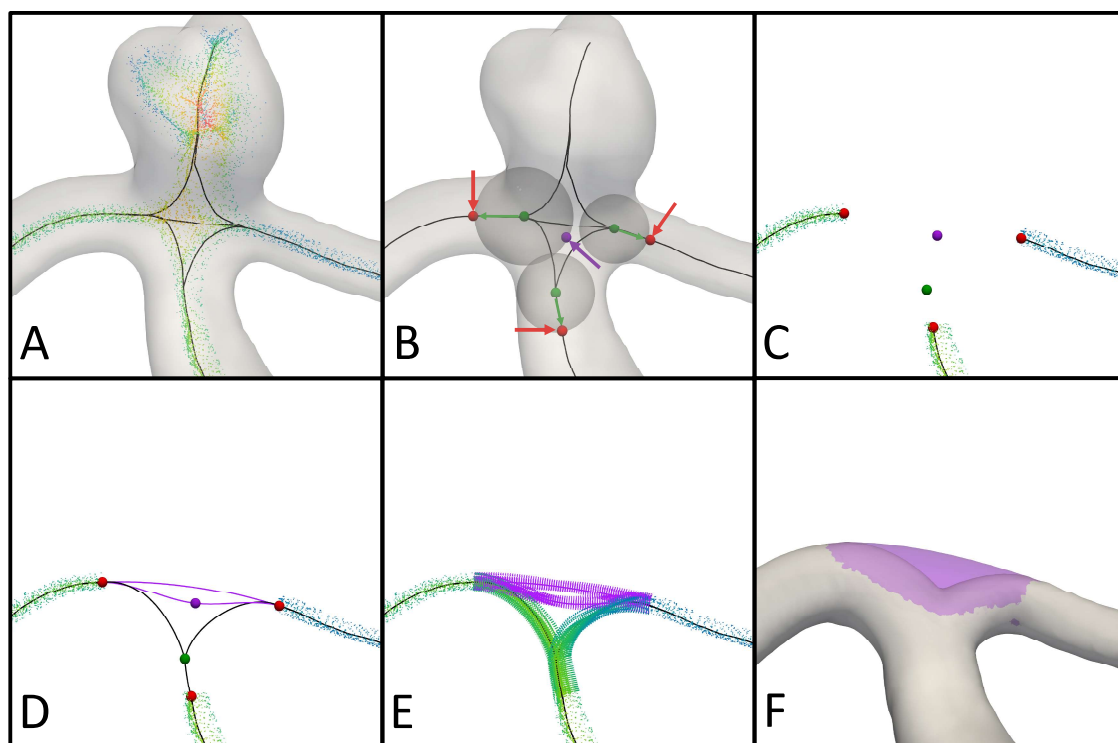


Figure 1: Illustration of the algorithm for removing a bifurcation aneurysm. The additions to the algorithm, relative to Ford et al., is highlighted in purple. Note that to ease comparison with Ford et al. we here illustrate the algorithm on the same model, but for the remainder of the paper we are applying the algorithm to bifurcations without aneurysms for validation purposes. **Step A**, compute the Voronoi diagram and five centerlines; two from the parent artery to each daughter branch, two from each daughter branch to the aneurysm sac, and one between the two daughter branches. **Step B**, the green dots are located where the centerlines coordinates diverge; referred to as diverging points, and the arithmetic mean of the coordinates of these is defined as the bifurcation center location, shown in purple. The diverging points are then moved one radius of the local minimal inscribed sphere away from the bifurcation center along the centerlines, as indicated by the green arrows; now referred to as clipping points. **Step C**, subtract the centerlines and Voronoi diagram that are located in between the clipping points. **Step D**, create a total of four new centerlines, two of which are passed through the diverging point from the parent artery to the daughter branches using third order splines. The remaining two start and end at the daughter branches, where one of them is passed through the bifurcation center. **Step E**, extrapolate the old Voronoi diagram along the new centerlines. **Step F**, envelope the Voronoi diagram to create a new surface.

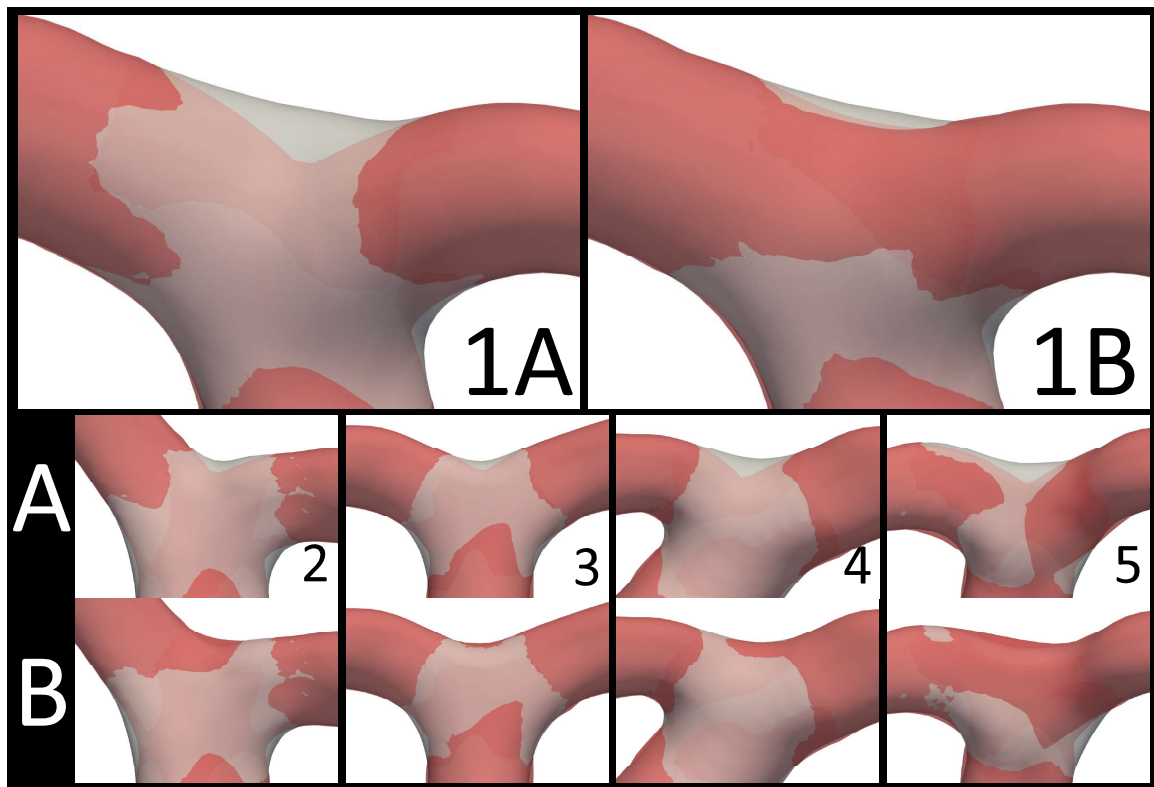


Figure 2: The figure shows the reference surface in opaque, with the results from the original and modified surface reconstruction algorithms colored in red in sub-plots A and B, respectively.

Figure3

[Click here to access/download;Figure;Figure3.pdf](#)

Figure 3 consists of two main panels, A and B. Panel A, labeled 'A', shows five rows of WSS maps for three models: Modified, Reference, and Ford. The rows are numbered 1 to 5. Each row contains three maps corresponding to the models. White lines indicate bifurcation lines. The color scale represents WSS magnitude, with red indicating higher values and blue indicating lower values. Panel B, labeled 'B', shows a 5x2 grid of line graphs. The columns are labeled 'WSS' and 'WSSG'. The rows correspond to the five bifurcation lines in panel A. The x-axis for all graphs is a normalized distance from 0.0 to 1.0. The y-axis for the 'WSS' column is in [Pa] and for the 'WSSG' column is in [Pa/mm]. A legend in the top right of panel B identifies the lines: blue for Modified, black for Reference, and orange for Ford.

Figure 3: **A** Wall shear stress (WSS) maps from computational fluid dynamic simulations of the modified, reference, and Ford models, from left to right, respectively, and bifurcation lines shown in white. The absolute values of the WSS are indicated in the panel to the right. **B** WSS and WSS gradients along the bifurcation lines where the colors black, orange, and blue refers to the modified, reference, and Ford models, respectively.

12

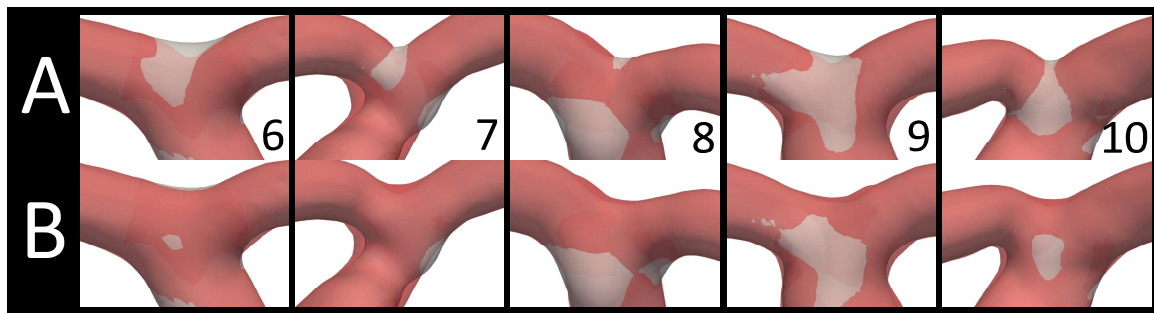


Figure 4: The figure shows the reference surface in opaque, with the results of the original and modified surface reconstruction algorithms colored in red in sub-plots A and B, respectively.

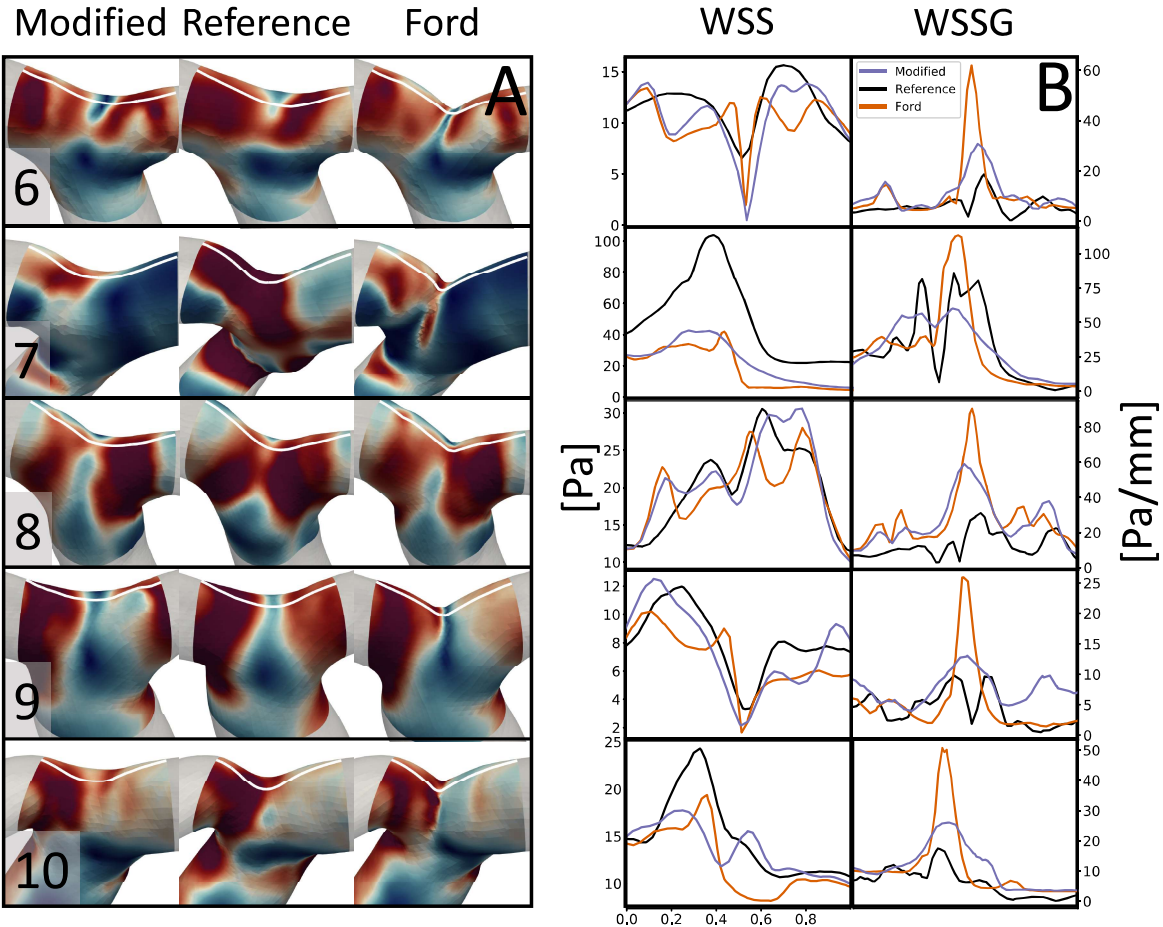


Figure 5: **A** Wall shear stress (WSS) maps from computational fluid dynamic simulations of the modified, reference, and Ford models, from left to right, respectively, and bifurcation lines shown in white. The absolute values of the WSS are indicated in the panel to the right. **B** WSS and WSS gradients along the bifurcation lines where the colors black, orange, and blue refers to the modified, reference, and Ford models, respectively.

Table1

Metric	Measure	Mean absolute error (SD)		p-value
		Ford	Modified	
Distance [mm]	Average	0.06 (0.03)	0.06 (0.04)	0.408
	Max	0.30 (0.15)	0.19 (0.11)	0.076
Curvature [$\frac{1}{mm}$]	Max	2.03 (0.48)	0.24 (0.26)	<0.001
WSS [Pa]	Average	7.27 (11.02)	5.63 (8.73)	0.037
	Max	17.57 (22.33)	12.90 (16.66)	0.081
WSSG [Pa/mm]	Average	12.54 (8.23)	9.41 (5.49)	0.012
	Max	50.22 (29.40)	26.82 (17.47)	0.001

Table 1: The table shows quantitative result based on the error measurements between the reference surface versus those obtained from the original and modified algorithms, respectively. P-values below 0.05 % are marked in bold.